Projections of South Asian Summer Monsoon under Global Warming from 1.5° to 5°C

ZHIBO LI,[a,b,c] YING SUN,[b,c] TIM LI,[d,c] WEN CHEN,[e,f] AND YIHUI DING[b]

[a] *Laboratory for Climate and Atmosphere–Ocean Studies, Department of Atmospheric and Oceanic Sciences, School of Physics, Peking University, Beijing, China*
[b] *National Climate Center, Laboratory for Climate Studies, China Meteorological Administration, Beijing, China*
[c] *Collaborative Innovation Center on Forecast and Evaluation of Meteorological Disasters (CIC-FEMD), Nanjing University of Information Science and Technology, Nanjing, China*
[d] *Department of Atmospheric Sciences, School of Ocean and Earth Science and Technology, University of Hawai'i at Mānoa, Honolulu, Hawaii*
[e] *Center for Monsoon System Research, Institute of Atmospheric Physics, Chinese Academy of Sciences, Beijing, China*
[f] *College of Earth and Planetary Sciences, University of Chinese Academy of Sciences, Beijing, China*

(Manuscript received 16 July 2020, in final form 29 June 2021)

ABSTRACT: The South Asian summer monsoon (SASM) is one of the most crucial climate components in boreal summer. The future potential changes in the SASM have great importance for climate change adaption and policy setting in this populous region. To understand the SASM changes and their link with the global warming of 1.5°–5°C above the preindustrial level, we investigate the changes in the SASM circulation and precipitation based on a large-ensemble simulation conducted with Canadian Earth System Model version 2 (CanESM2). With the global mean surface temperature (GMST) increase, the large-ensemble mean of SASM circulation is projected to weaken almost linearly while the precipitation and precipitable water are projected to enhance quasi-linearly. A double anticyclone along the tropical Indian Ocean is a major anomalous circulation pattern for each additional degree of warming and is responsible for the weakening of the lower-level westerlies. The decreased upper-level land–sea thermal contrast (TC_{upper}) is the main thermal driver for the weakening of the SASM circulation while the lower-level thermal contrast contributes little. The nonlinearly decreased TC_{upper} is mainly related to the temperature response to the increased CO_2 forcing and convection-induced latent heat release in the tropics. The increase in the SASM precipitation is mainly due to the quasi-linearly increased positive contribution of the thermodynamic component, while the dynamic component has a negative impact. Both horizontal moisture advection and moisture convergence contribute to the precipitation increase, and moisture convergence plays a dominant role. These results provide new insight that the SASM changes can be roughly scaled by the GMST changes.

KEYWORDS: Monsoons; Precipitation; Climate change; Water budget/balance; Climate prediction

1. Introduction

The South Asian summer monsoon (SASM) is a crucial part of the global monsoon and impacts more than one billion people's lives. With global warming, the SASM experienced substantial changes and has exerted serious impacts on the ecosystem and social economy in South Asia. Many observations have demonstrated a negative trend in the Indian monsoon precipitation from 1950 to 2000 (Parthasarathy et al. 1994; Mitchell and Jones 2005; Ramanathan et al. 2005; Turner and Annamalai 2012), with a decrease in moderate rainfall events (Rajeevan et al. 2006) but an increase in heavy precipitation over central India (Gautam et al. 2009). Jin and Wang (2017) used multiple observational datasets and found a significant recovering wet trend in the rainfall over central India during the monsoon season since 2002. On the other hand, the intensity of the SASM circulation is found to be weakened from the 1950s together with a weakening local meridional circulation (Wang et al. 2020a,b).

Different factors are linked to the weakening of SASM precipitation from the 1950s to 2000s, including changes in meridional thermal contrast (Xavier et al. 2007; Dai et al. 2013), black carbon and/or sulfate aerosols (Chung and Ramanathan 2007; Lau et al. 2008; Bollasina et al. 2011; Zhou et al. 2020), land use (Niyogi et al. 2010), and sea surface temperature (SST) change (Annamalai et al. 2013; Huang et al. 2020a; Yang and Huang 2021). Xavier et al. (2007) proposed that thermodynamic conditions associated with the change of sign of upper-level tropospheric temperature gradient from negative to positive set up conditions for triggering symmetric instability, large-scale organized convection, and the dynamic SASM onset. Bollasina et al. (2011) emphasized the differential cooling effects from anthropogenic aerosols of the source and nonsource regions, and reduction in the land–sea surface thermal contrast as the main mechanisms of the weakening of SASM circulation. On the other hand, the revival of SASM precipitation since 2002 is closely related to an enhanced land–sea thermal contrast, driven by strong warming over the Indian subcontinent and weaker warming over the Indian Ocean (Jin and Wang 2017).

Denotes content that is immediately available upon publication as open access.

Corresponding author: Ying Sun, sunying@cma.gov.cn

DOI: 10.1175/JCLI-D-20-0547.1

For the observed changes in the SASM, the models from phase 5 of the Coupled Model Intercomparison Project (CMIP5) show good and improved skill in simulating monsoon variability compared to CMIP3 models (Sperber et al. 2013). The SASM is projected to have an increased precipitation but a decreased circulation under global warming (Ueda et al. 2006; Sun et al. 2010; Christensen et al. 2013; IPCC 2013). The enhanced atmospheric water vapor content (Douville et al. 2000) and the increased atmospheric moisture convergence into the South Asia region (May 2004) are thought to be responsible for the increase of precipitation (Ueda et al. 2006; Cherchi et al. 2011; May 2011). Wang et al. (2013) used 20 CMIP5 models and found that the interaction of the increased water vapor and increased static stability lead to that the change of monsoon precipitation is less than what expected from the increasing water vapor content. Endo and Kitoh (2014) used CMIP5 models and found that the thermodynamic component corresponding to the ''wet-get-wetter'' effect has the most positive contribution to SASM precipitation increase, while the dynamic component largely offsets the thermodynamic component because of a slowdown of the overturning circulation. Li and Ting (2017) found the SASM precipitation increase is dominated by the direct CO_2 radiative effect (fast component), while the response to SST warming (slow component) shows large uncertainty among CMIP5 models. Lee et al. (2018) pointed out that SASM precipitation change is determined by the increase in evaporation and the thermodynamic component at 1.5° and 2°C warming based on five atmospheric global climate models. For SASM circulation, most coupled global climate models suggested a weakened SASM circulation despite increased near-surface land–sea thermal contrast (Ueda et al. 2006; Sun et al. 2010; Christensen et al. 2013). Sun et al. (2010) suggested that the enhanced upper-tropospheric warming over the tropical Indian Ocean plays a crucial role in SASM circulation change. The enhanced latent heating from tropical convection weakens the meridional (tropical Indian Ocean and Tibetan Plateau) thermal contrast, which favors the weakened SASM circulation. Chen and Zhou (2015) pointed that the SST warming over the western central Pacific plays an important role in modulating the SASM lower-level circulation through the Gill response.

With the progress in international climate negotiations, it has become a global consensus to avoid a global temperature rise of 2°C above the preindustrial period. Some recent studies investigated the SASM changes at specific temperature thresholds of 1.5° and 2°C of warming. Chevuturi et al. (2018) found an increase in summer monsoon precipitation over South Asia. Zhang et al. (2018) showed evidence that limiting global warming to 1.5°C instead of 2°C would robustly reduce areal and population exposures to dangerous extreme precipitation events, especially in South Asian monsoon regions. Bhowmick et al. (2019) evaluated the impact of every 0.5°C increments in global warming over South Asia and found an increase in maximum and median values of the summer mean precipitation over Indian land areas. Dry regions are projected to become drier and wet regions are projected to become wetter with the increase in warming, except over the Bay of Bengal. However, very few studies investigate the SASM changes under specific global warming levels when the global mean surface temperature (GMST) is over 2°C of warming (Bhowmick et al. 2019).

These previous studies illustrate the future changes in the SASM circulation and precipitation under different emission scenarios based on multimodel ensembles. However, rare studies investigate the SASM changes from 1.5° to 5°C warming, which helps understand the response of the SASM to different temperature rises above the preindustrial level (Cherchi et al. 2011; Chen and Zhou 2015). It is also one of the central issues in the current international climate change negotiation including the Paris agreement. The GMST-based projection not only serves as the scientific basis for the development of temperature rise target but also helps understand if the SASM changes can be scaled by the GMST as happens for some other variables, which have shown a linear relationship with the mean temperature changes (Li et al. 2019; Seneviratne and Hauser 2020). Therefore, here we use a large ensemble runs with the Canadian Earth System Model version 2 (CanESM2) to investigate the link between the SASM circulation and precipitation changes and the specific warming levels. The large ensemble is designed to tackle the forced response versus internal variability and the model results avoids the problems arising from inconsistent definition of the GMST changes relative to the preindustrial period (Mitchell et al. 2017; Deser et al. 2020). It ensures a good enough sampling to make the model ensemble and investigate the climate change under specific warming levels. Besides, the large-ensemble model also has good ability to extract the forced signal versus the internal variability (Deser et al. 2020; Huang et al. 2020b; Lehner et al. 2020; Li et al. 2021).

The paper is structured as follows. The data and methods are described in section 2. Projections of the SASM system under different global warming levels are given in section 3. In section 4, we use two moisture budget methods to calculate the relative contributions of thermodynamic and dynamic components to the SASM precipitation changes. The conclusions are summarized in section 5.

2. Data and methods

a. *Observational and model data*

In the present study, we used four observational datasets: 1) monthly precipitation data from the Global Precipitation Climatology Project (GPCP V2.3; Adler et al. 2003), 2) monthly precipitation data from the Center for Climate Prediction Merged Analysis of Precipitation (CMAP; Xie and Arkin 1997), 3) monthly datasets (zonal winds, meridional winds, and precipitable water) from the European Centre for Medium-Range Weather Forecasts Reanalysis (ERA-Interim; Dee et al. 2011), and 4) monthly datasets (zonal winds, meridional winds, and precipitable water) from the National Centers for Environmental Prediction (NCEP1; Kalnay et al. 1996). The horizontal resolution of the data is 2.5° × 2.5° for GPCP V2.3, CMAP, and NCEP1, whereas it is 1.5° × 1.5° for ERA-Interim. All of the observational datasets were interpolated onto T42 (approximately 2.81°) resolution, which is consistent with the resolution

of CanESM2. The analyses are performed on all of the variables from 1979 to 2016.

The model data are from large-ensemble runs of CanESM2 (Arora et al. 2011), which includes 50 ensemble members. The simulations are driven by historical anthropogenic and natural external forcing for 1950–2005 and the representative concentration pathway (RCP) 8.5 scenario (the high emissions pathway toward 8.5 W m^{-2} in 2100) for 2006–2100 for different initial conditions (Fyfe et al. 2017). The CanESM2 models comprises four parts: 1) an atmospheric model (CanAM4; von Salzen et al. 2013), 2) an ocean model (CanOM4; Arora et al. 2011), 3) a terrestrial carbon model (CTEM; Arora et al. 2009; Arora and Boer 2010), and 4) an ocean carbon model (CMOC; Arora and Boer 2010). Since the large ensemble runs of CandESM2 start from 1950, to calculate the GMST changes relative to the preindustrial period (1850–1900) we also used the five-member ensemble of CanESM2 from CMIP5 between 1850 and 1950.

b. Global warming levels

Two baseline periods are used to estimate future changes in the SASM metrics. The first one is defined as the preindustrial period from 1850 to 1900, which is used to estimate specific global warming levels relative to the preindustrial period. Since only the CanESM2 provides the data after 1950, the 10-yr mean temperatures from the CanESM2 between 1850 and 1900 are removed to define the different warming levels. Based on this, the six time periods with 10-yr mean temperature increase from 1° to 5°C are defined as follows: 1995–2004 (0.983°C), 2007–16 (1.454°C), 2021–30 (1.981°C), 2042–51 (2.958°C), 2061–70 (3.978°C), and 2079–88 (4.980°C). The six time periods demonstrate not real equilibrium, but transient climate responses at 1°–5°C of warming. The second baseline period is the current climate (also the 1°C warming compared to the preindustrial period) from 1995 to 2004 in the model world, which is used to define future changes relative to the current climate. The definition of the current climate is consistent with the observed GMST changes in 2018/19 of approximately 1°C above preindustrial level (Sun et al. 2018; WMO 2020). Hereafter, the GMST warming levels from 1° to 5°C changes are relative to the preindustrial period, while the SASM changes are relative to the current climate. We also tested the sensitivity of our results to the different baseline periods. We found the use of different baseline periods, including the preindustrial period and the current climate as the baseline for future changes, would not affect the overall conclusions about future SASM changes. We also use the Student's t test to conduct the significance test for the changes in SASM relative to the current climate.

c. SASM indices and land–sea thermal contrast

Previous studies used different indices to define the SASM intensity (Webster and Yang 1992; Goswami et al. 1999; Wang and Fan 1999; Goswami and Xavier 2005). Webster and Yang (1992) defined a circulation index (Webster–Yang index) based on zonal wind shear between 850 and 200 hPa, averaged over South Asia in the region of 40°–110°E, 0°–20°N. This index reflects the combined strength in both the lower and upper troposphere zonal winds and the north–south land–sea thermal contrast (Dai et al. 2013). Xavier et al. (2007) defined a large-scale tropospheric temperature gradient to analyze the SASM onset and withdrawal date. The all-India summer rainfall index (June–September averaged precipitation over India) is used to measure the Indian summer monsoon (Parthasarathy et al. 1994). However, Wang and Fan (1999) suggested that this rainfall index only reflects the strength of the monsoon rain over India, not the large-scale summer monsoon precipitation in South Asia.

Dai et al. (2013) showed the variations and changes in thermal contrast in the mid-upper (200–500 hPa) troposphere (TC_{upper}), and thermal contrast in the mid-lower (500–700 hPa) troposphere (TC_{lower}) are highly correlated with the strength of the SASM circulation. They also quantified the relative roles of the TC_{upper} and TC_{lower} in driving the SASM circulation and emphasized the latent heating from monsoon rainfall can affect the land–sea thermal contrast, which provides strong feedback for the SASM circulation. Following their definition, in our paper, the SASM circulation index (SASMI) and north–south (TC_{upper} and TC_{lower}) land–sea thermal contrasts in the upper and lower troposphere in the SASM region are defined as follows:

$$\mathrm{SASMI} = U(850\,\mathrm{hPa}; 60°\text{–}100°\mathrm{E}, 0°\text{–}20°\mathrm{N}) - U(200\,\mathrm{hPa}; 60°\text{–}100°\mathrm{E}, 0°\text{–}20°\mathrm{N}), \quad (1)$$

$$\mathrm{TC}_{\mathrm{upper}} \approx Z(200\text{–}500\,\mathrm{hPa}; 60°\text{–}100°\mathrm{E}, 20°\text{–}40°\mathrm{N}) - Z(200\text{–}500\,\mathrm{hPa}; 60°\text{–}100°\mathrm{E}, 10°\mathrm{S}\text{–}10°\mathrm{N}), \quad (2)$$

$$\mathrm{TC}_{\mathrm{lower}} \approx Z(500\text{–}700\,\mathrm{hPa}; 60°\text{–}100°\mathrm{E}, 20°\text{–}40°\mathrm{N}) - Z(500\text{–}700\,\mathrm{hPa}; 60°\text{–}100°\mathrm{E}, 10°\mathrm{S}\text{–}10°\mathrm{N}), \quad (3)$$

where U denotes the zonal winds and Z denotes the geopotential height. The north region denotes land, the south region denotes sea, and the difference between north and south boxed regions (blue boxes in Fig. 1b) represents the land–sea thermal contrast. We use the vertical mean to calculate TC_{upper} and TC_{lower}. And we use the thermal contrast indices to discuss the physical mechanisms of the SASM circulation changes. Besides, we use the area-averaged JJA precipitation over 60°–100°E, 0°–20°N (red boxes in Fig. 1) to represent the SASM precipitation changes, which is the same as the region of SASMI. Although the definition is a little different from previous works (Wang and Fan 1999; Wang et al. 2012), the effects from circulation changes on precipitation can cooperate well with other variables (such as precipitable water and static stability).

To quantify the percentage changes in the SASM metrics, we calculated the difference of each variable between two adjacent warming levels, which is then divided by the mean value at the first level. We also use locally estimated scatterplot smoothing (loess) regression (Cleveland 1979) to define the linear and nonlinear change of the SASM metrics. A "linear or quasi-linear change" denotes that the loess regression line is basically like a straight line without any curve, while a "nonlinear change" denotes that the loess regression line clearly shows a curve.

d. Two moisture budget methods

Previous studies diagnosed relative contributions from thermodynamic (atmospheric specific humidity) and dynamic (circulation)

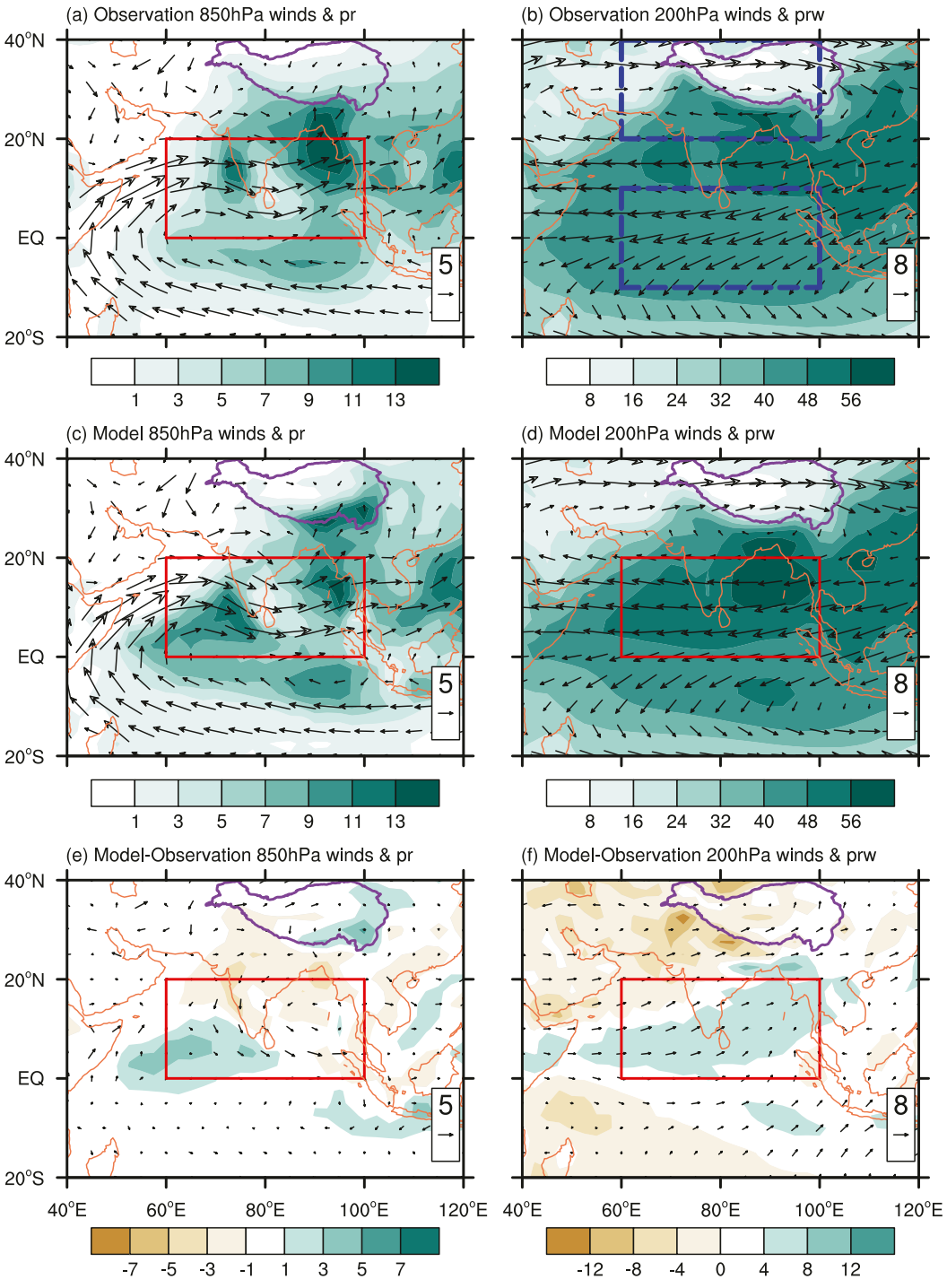

FIG. 1. (a),(c) 850-hPa winds and precipitation and (b),(d) 200-hPa winds and precipitable water from (top) observations (1986–2015) and (middle) CanESM2 (1977–2006) in June–August (JJA) when both observed and model-simulated GMST is increased by 1°C above the preindustrial levels (1850–1900). (e),(f) As in (a) and (b), but for model minus observation. Observed winds (vector; m s^{-1}) and precipitable water (shading; kg m^{-2}) based on the mean of ERA-Interim and NCEP1, and precipitation (shading; mm day^{-1}) based on the mean of GPCP and CMAP. Model-simulated variables are the 50-run ensemble mean of CanESM2. Red solid boxes represent the SASM key area (0°–20°N, 60°–100°E). Blue dotted boxes in (b) represent the regions (north: 60°–100°E, 20°–40°N, south: 60°–100°E, 10°S–10°N) used in calculating TC_{upper} and TC_{lower}. The Tibetan Plateau is masked by purple solid lines.

components to precipitation changes under global warming based on column-integrated (Held and Soden 2006; Chou et al. 2009; Seager et al. 2010; Hsu et al. 2012, 2013; Li and Ting 2017; Jin et al. 2020) and simplified (Huang et al. 2013; Huang and Xie 2015; Sooraj et al. 2015; Zhou et al. 2017; Li et al. 2019) formulas. Here, we use two methods to discuss the precipitation changes in the SASM region. The first one is the moisture budget decomposition proposed by Hsu et al. (2012):

$$\Delta P = -\Delta\frac{1}{g}\int_{\mathrm{ps}}^{100\,\mathrm{hPa}}\left(u\frac{\partial q}{\partial x}+v\frac{\partial q}{\partial y}\right)dp-\Delta\frac{1}{g}\int_{\mathrm{ps}}^{100\,\mathrm{hPa}}q\left(\frac{\partial u}{\partial x}+\frac{\partial v}{\partial y}\right)dp+\Delta E, \tag{4}$$

$$\Delta\mathrm{AD} = -\Delta\frac{1}{g}\int_{\mathrm{ps}}^{100\,\mathrm{hPa}}\left(u\frac{\partial q}{\partial x}+v\frac{\partial q}{\partial y}\right)dp\,, \tag{5}$$

$$\Delta\mathrm{MC} = -\Delta\frac{1}{g}\int_{\mathrm{ps}}^{100\,\mathrm{hPa}}q\left(\frac{\partial u}{\partial x}+\frac{\partial v}{\partial y}\right)dp, \tag{6}$$

where Δ denotes the difference between future and current climate; ΔP denotes the precipitation change, g denotes the acceleration of gravity ($9.8\,\mathrm{m\,s^{-2}}$), ps denotes surface pressure, p denotes pressure, u and v denote the horizontal zonal and meridional winds, respectively, q is the specific humidity, E is evaporation, and $\int_{\mathrm{ps}}^{100\,\mathrm{hPa}}$ denotes the total column integration from surface pressure to 100 hPa. The three terms on the right-hand side of the Eq. (4) represent the horizontal advection [ΔAD; Eq. (5)], moisture convergence [ΔMC; Eq. (6)], and surface evaporation (ΔE), respectively.

As the changes of atmospheric water vapor and circulation can affect the moisture convergence, it is crucial to investigate the relative contribution of thermodynamic component and dynamic component to precipitation change. The term ΔMC can be decomposed into three terms as shown:

$$\Delta\mathrm{MC} = -\int_{\mathrm{ps}}^{100\,\mathrm{hPa}}\left[\overline{q}\Delta\left(\frac{\partial u}{\partial x}+\frac{\partial v}{\partial y}\right)+\Delta q\overline{\left(\frac{\partial u}{\partial x}+\frac{\partial v}{\partial y}\right)}+\Delta q\Delta\left(\frac{\partial u}{\partial x}+\frac{\partial v}{\partial y}\right)\right]dp, \tag{7}$$

$$\Delta\mathrm{DY} = -\int_{\mathrm{ps}}^{100\,\mathrm{hPa}}\left[\overline{q}\Delta\left(\frac{\partial u}{\partial x}+\frac{\partial v}{\partial y}\right)\right]dp, \tag{8}$$

$$\Delta\mathrm{TH} = -\int_{\mathrm{ps}}^{100\,\mathrm{hPa}}\left[\Delta q\overline{\left(\frac{\partial u}{\partial x}+\frac{\partial v}{\partial y}\right)}\right]dp, \tag{9}$$

$$\Delta\mathrm{NL} = -\int_{\mathrm{ps}}^{100\,\mathrm{hPa}}\left[\Delta q\Delta\left(\frac{\partial u}{\partial x}+\frac{\partial v}{\partial y}\right)\right]dp. \tag{10}$$

The overbar denotes the values for the current climate. The first term on the right side of the Eq. (7) is associated with the circulation {divergence; $\Delta[(\partial u/\partial x)+(\partial v/\partial y)]$} change, which indicates a dynamic component [ΔDY; Eq. (8)]. The second term means the change of water vapor content (Δq), which reflects the contribution of the thermodynamic component [ΔTH; Eq. (9)]. The third term is a nonlinear term [ΔNL; Eq. (10)], which includes the nonlinear effect of both dynamic and thermodynamic components. At first, we calculated each term at each grid point. Then, the weighted area average is used to calculate the value of each term.

Besides, we also use a simplified moisture budget decomposition proposed by Huang et al. (2013):

$$\Delta P = -\frac{1}{\rho g}(\overline{q}_s\Delta\omega+\Delta q_s\overline{\omega}), \tag{11}$$

where q_s denotes surface specific humidity and ω denotes the pressure velocity at 500 hPa. The simplified moisture budget method can generally be used to directly demonstrate the dynamic (vertical motion) and thermodynamic (water vapor) components of precipitation changes over the tropics (Huang et al. 2013; Huang and Xie 2015) and help us to understand the SASM precipitation changes in a different way. We should note that both methods cannot completely separate the contributions from dynamic and thermodynamic components due to the possible interaction between lower-level water vapor and vertical motion changes.

e. Model evaluation in simulating the SASM system

Figure 1 shows that the model generally reproduces the spatial patterns of observed circulations at 850 and 200 hPa, and so do the precipitation and precipitable water content. There are two precipitation centers in the SASM region (red box): one is over the seashore of southwest India and the other one is over the Bay of Bengal. The model well captures the observed lower-level southwesterly airflows from the Indian Ocean to the South China Sea and upper-level easterly airflows over South Asia. The model also well simulates the cross-equatorial flow over the tropical oceans, which is consistent with the findings by Li et al. (2019). Compared with the observations, the model overestimates the precipitation over the tropical western Indian Ocean and southeastern Tibetan Plateau and underestimates the precipitation over the Indian subcontinent and the Bay of Bengal. The correlation coefficients between the observed and model-simulated precipitation and zonal winds in the SASM region are 0.70 and 0.90, respectively. All these suggest that the model well captures the basic large-scale features of the SASM, although some deficiencies are seen especially in the high-terrain regions.

3. Future changes in the SASM under 1.5°–5°C of warming

a. Spatial distribution

Figure 2 shows the spatial patterns of changes in SASM 850-hPa winds and precipitation (Figs. 2a–e), as well as in 200-hPa winds and precipitable water (Figs. 2g–k), under 1.5°–5°C of warming. At 1.5°C of warming, there are anomalous lower-level easterly winds over the equator in the Northern Hemisphere. When the GMST increases more than 2°C above the preindustrial level, it becomes clear that the easterly winds are quite strong and divided into two branches flowing northward and southward around 60°E, with a clear double anticyclone pattern located along the equator. The anomalous easterly winds over the tropical Indian Ocean around 0°–10°N suppress the

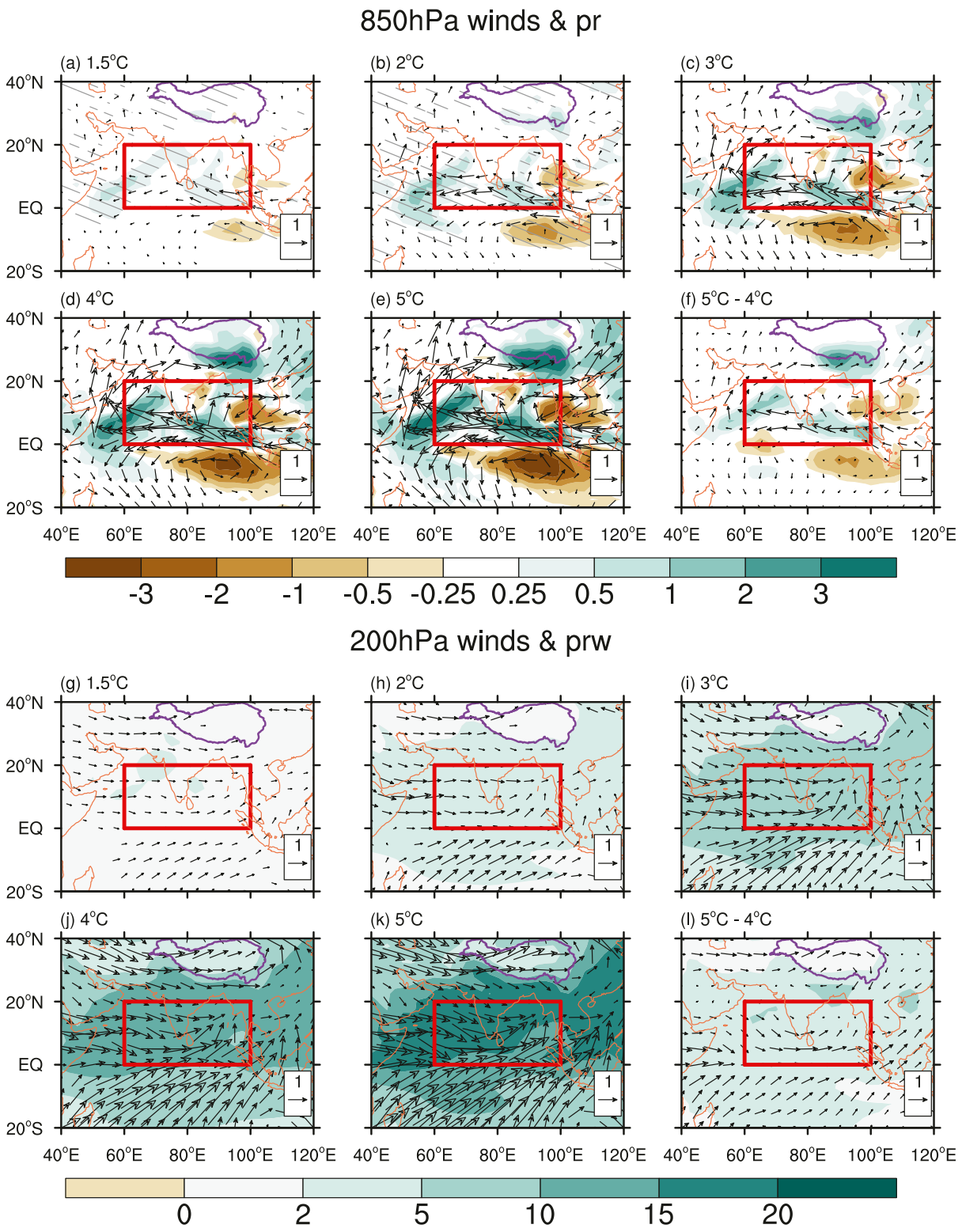

FIG. 2. (a)–(e) Changes (relative to the current climate, mean of 1995–2004) of 850-hPa winds (vector; m s^{-1}) and precipitation (shading, mm day^{-1}) in JJA when global warming is at 1.5°C (2007–16), 2°C (2021–30), 3°C (2042–51), 4°C (2061–70), and 5°C (2079–88) above the preindustrial levels, respectively. (f) As in (a)–(e), but for differences between 5° and 4°C. (g)–(k) As in (a)–(e), but for changes in 200-hPa winds (vector; m s^{-1}) and precipitable water (shading; kg m^{-2}). (l) As in (g)–(k), but for differences between 5° and 4°C. Dark gray slashes in (a) and (b) denote the changes in precipitation that are significant at the 0.05 level. The changes in precipitation and precipitable water are nearly significant at each grid point in (c)–(e) and (g)–(k). Vectors denote the changes in 850- and 200-hPa winds that are significant at the 0.05 level. Red solid boxes represent the SASM precipitation area (0°–20°N, 60°–100°E). The Tibetan Plateau is masked by purple solid lines.

climatology westerly winds near the Indian continent, which is the main reason for the weakening of the SASM lower-level circulation. This spatial pattern of lower-level winds is very similar to that in Li et al. (2015) based on CMIP5 models. For the precipitation changes, there is increased precipitation over the northern Indian Ocean. The precipitation anomalies center around 80°–100°E induce the double anticyclone pattern because of Rossby wave response, indicating a close relationship between the weakening of the SASM circulation and the tropical precipitation anomaly. In the upper troposphere, the anomalous westerly winds are projected to enhance continuously in the SASM region (Figs. 2g–k). The weakened tropical easterly jet (TEJ) indicates the weakening of the upper-level SASM circulation. On the other hand, precipitable water will significantly increase with global warming, with the maximum increase located at the north of the equator (SASM region), which provides a favorable condition for the precipitation increase in the region. Besides, the changes for each additional degree of warming (we only show the differences between 5° and 4°C) show similar spatial patterns, with a double lower-level anticyclone located around the negative precipitation center (Fig. 2f) and weakened upper-level SASM circulation (Fig. 2l). The similar spatial patterns suggest that the SASM circulation and precipitation will change roughly linearly with the GMST increase.

Figures 3a–e show the spatial patterns of changes in vertically integrated water vapor flux and static stability. The spatial patterns of changes in water vapor transport over the Asian continent are very similar to that in 850-hPa winds (Figs. 2a–e). A clear anomalous water vapor transport belt is seen over northern India passing through the Somali jet. This provides favorable moisture conditions for the occurrence of anomalous precipitation in the tropical Indian Ocean. The static stability significantly increases over most land regions when global warming is above 2°C. The increasing rate of static stability is larger over land than that over the ocean because of a strong warming center over the tropics in the upper layer (see Fig. 7). Enhanced static stability may suppress local convection and conducive to precipitation decrease, which plays a counteracting role with the increased precipitable water (Figs. 2g–k) in precipitation change. Figures 3g–k further show changes in the longitude–height cross section of vertical circulation averaged along 0°–20°N from 1.5° to 5°C of warming. The upper-layer TEJ will be weakened significantly with warming. There will be an anomalous ascending motion over the tropical western Indian Ocean and an anomalous descending motion around 80°–100°E, which corresponds to increased and decreased precipitation centers, respectively. The enhancement of this anomalous vertical circulation suggests a weakened Walker circulation, which links to the weakening of the SASM circulation in both upper and lower levels.

b. *SASM metrics*

Figure 4 shows future changes in the four SASM metrics and their links with the GMST changes. The large-ensemble mean results show that the SASMI (Fig. 4a) is projected to decrease quasi-linearly with global warming while the precipitation (Fig. 4b) and precipitable water (Fig. 4c) will increase quasi-linearly. The spread among different runs is quite large for precipitation compared with the mean response of the model, which reflects the important role of internal variability in the future change of SASM precipitation. The decrease of SASMI is due to the weakening of both the lower-level westerlies and the upper-level TEJ while the precipitation increase is mainly related to the increased precipitable water and moisture transport. The static stability (Fig. 4d) will increase nonlinearly with a slower rate at higher warming levels, which contributes to changes in both circulation and precipitation. The change in the stability is closely related to the amplified warming in the upper troposphere in response to increased CO_2 forcing, especially in the tropics (IPCC 2013). Table 1 shows the quantified relation between these metrics and GMST. The SASM precipitation increases by 3.5%, 4.2%, 3.6%, and 3.4% K^{-1} from 1° to 2°C, from 2° to 3°C, from 3° to 4°C, and from 4° to 5°C, respectively. Meanwhile, the changes in global precipitation are 1.6%, 1.3%, 1.1%, and 1.1% K^{-1} for each degree of warming from 2° to 5°C, respectively. Compared with the global mean, the monsoon precipitation increase in the SASM region is 2–3 times more, which reflects the ''wet get wetter'' characteristics in the wet monsoon region. The change in precipitable water is quite close to the global mean (~7% K^{-1}), which is consistent with the estimate of ~7% K^{-1} based on the Clapeyron-Clausius equation (Held and Soden 2006), indicating the change of water vapor mainly following the thermal changes of mean temperature. The increasing rate of precipitable water is higher than that of precipitation, which also indicates the intensity of the hydrologic cycle is controlled not only by the precipitable water, but by the availability of energy (Allen and Ingram 2002). All these depict a picture of future SASM changes with roughly linear increase in precipitation and decrease in circulation, suggesting a quasi-linear scaling relation with the GMST increases. Besides, probability density functions indicate that the variabilities of the SASM circulation and precipitation will not change much (not shown).

The upper- and lower-layer thermal contrasts TC_{upper} (Fig. 5a) and TC_{lower} (Fig. 5b) are calculated to understand the dynamical mechanisms causing the SASM circulation change. With the GMST increase, TC_{upper} will decrease nonlinearly while TC_{lower} will slightly increase. The results are quite similar when the different baseline periods are used. The decrease of TC_{upper} is consistent with the roughly linear decrease in 200-hPa zonal winds (not shown), indicating that the weakened thermal contrast in the upper troposphere plays a dominant role in driving the decrease in TEJ in the SASM region. We note that the decrease in TC_{upper} may reflect two characteristics: one is related to the response of the tropical upper-layer temperature to the increased greenhouse gases (Turner and Annamalai 2012), while the other one is related to strong latent heat release from the anomalous enhanced precipitation in the tropical Indian Ocean, which is more than those at the midlatitude Asian continent (Figs. 2a–e). All these lead to a more rapid warming in the upper troposphere in the tropics than in the subtropical regions. The nonlinear decrease of the TC_{upper} and almost linear decrease of SASM circulation indicate that important feedback may exist between the circulation and precipitation in the SASM changes. The decreased upper-layer land–sea thermal contrast induces the decreased circulation; on the

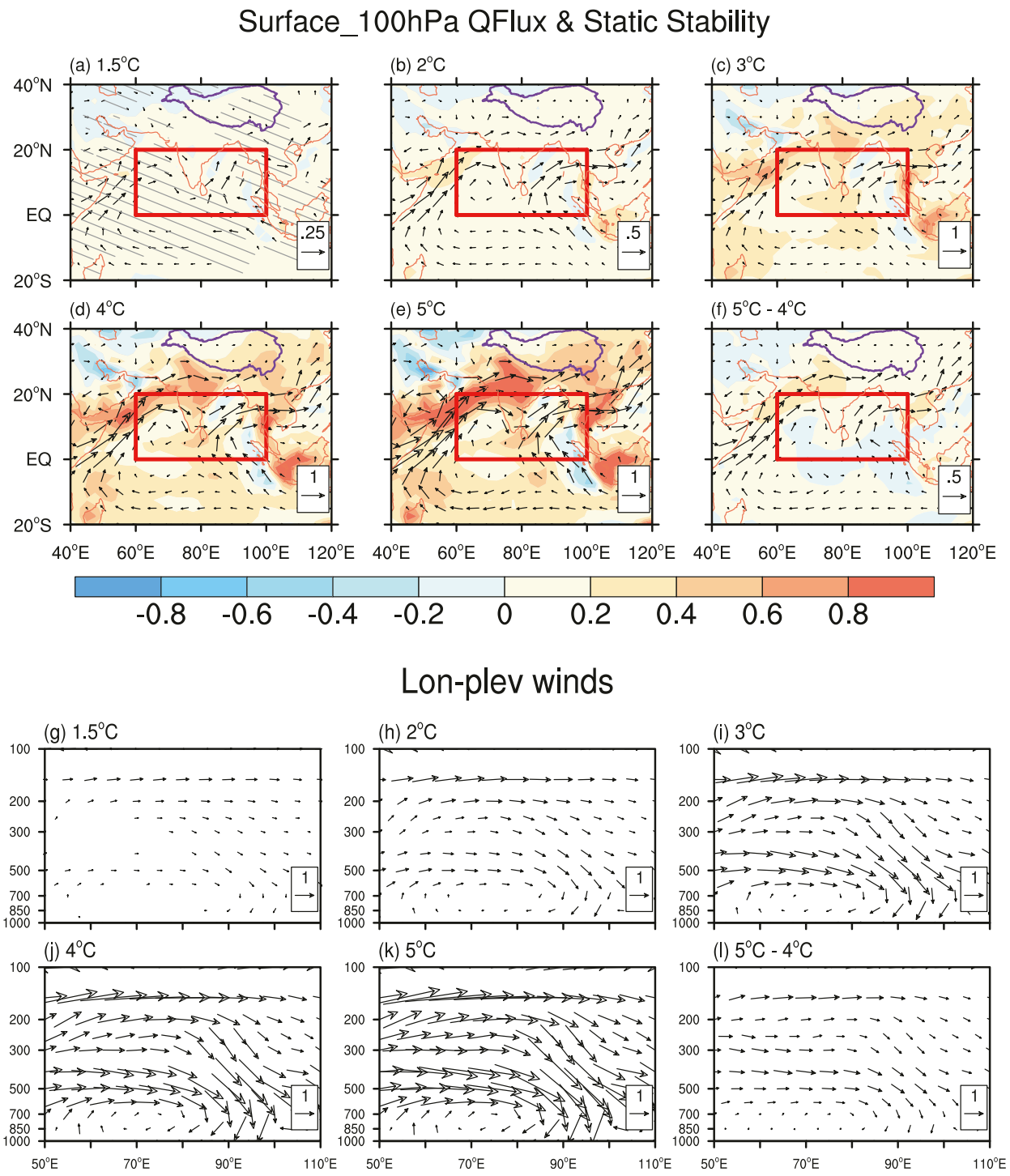

FIG. 3. As in Figs. 2a–f, but for (a)–(f) surface to 100-hPa integral water vapor transport (vector; kg m^{-1} s^{-1} hPa^{-1}) and static stability (shading; potential temperature $\theta_{400\text{–}300\,hPa} - \theta_{1000\text{–}850\,hPa}$; K), and (g)–(l) meridional averaged (0°–20°N) vertical motion (m s^{-1} for zonal velocity and $\times 10^{-2}$ Pa s^{-1} for vertical velocity). Dark gray slashes in (a) denote the changes in static stability that are significant at the 0.05 level. The changes of static stability are nearly significant at each grid point in (b)–(e). Vectors denote the changes in water vapor transport and winds are significant at the 0.05 level.

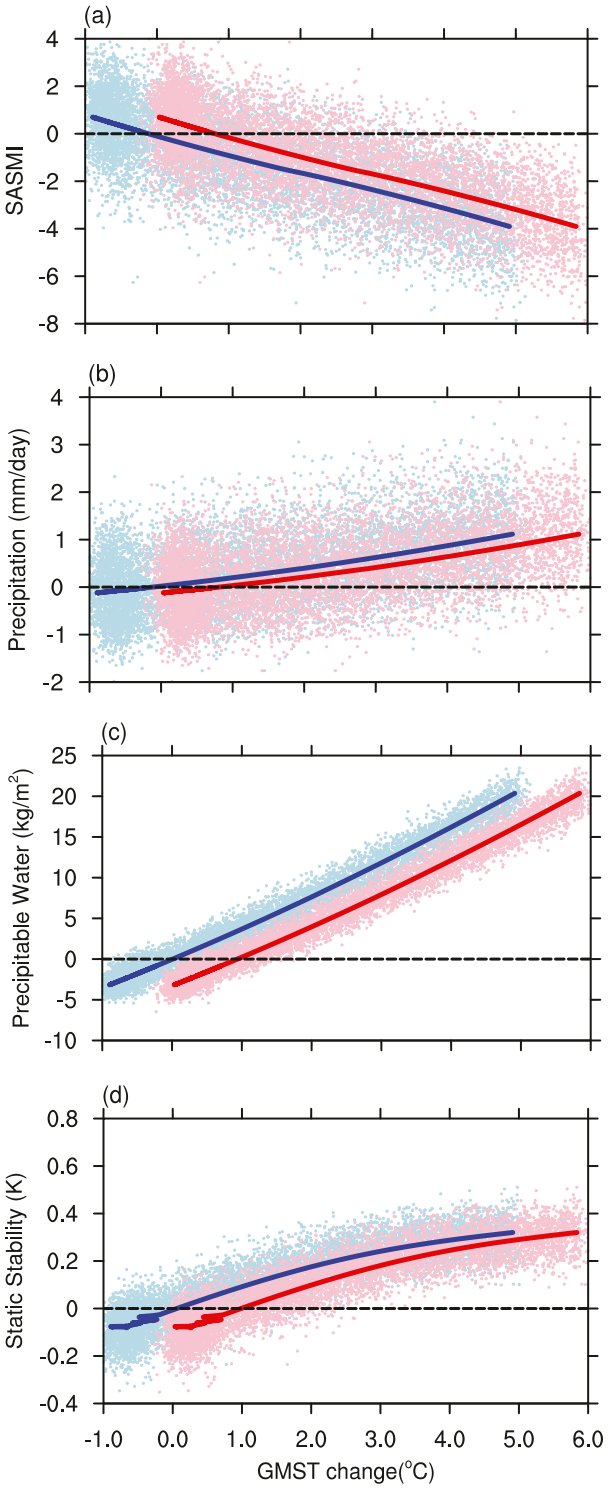

FIG. 4. Scatterplots of the relationships between the JJA average of (a) the SASMI and, resepectively, the SASM area-averaged (0°–20°N, 60°–100°E) (b) precipitation (mm day^{-1}), (c) precipitable water (kg m^{-2}), and (d) static stability (K) and GMST (°C). Light blue dots and blue solid lines denote the changes in the SASM metrics and GMST are relative to the current climate (1995–2004). Pink dots and red solid lines denote that changes in the SASM metrics are relative to the current climate and GMST is relative to the preindustrial period (1850–1900). The solid lines denote the 50-run ensemble mean of CanESM2 with loess smoothing.

other hand the precipitation can be enhanced by the increased moisture, which in turn offsets the decrease of land–sea thermal contrast. Figure 6 shows the changes in zonally averaged air temperature over the SASM region. The most prominent warming is located in the tropical area, and the warming decreases gradually from the equator to the polar regions. It is known that the summer climatological upper-level troposphere temperature over the South Asian continent is warmer than that of the tropical Indian Ocean (Webster et al. 1998; Dai et al. 2013). As a result, the upper-level land–sea thermal contrast will decrease in the future (Fig. 5a), which leads to a decrease in the TEJ and SASM circulation (Fig. 2). The increase of TC_{lower} can be related to the combined effects of faster near-surface air warming over the continent than the Indian Ocean according to the difference in heat capacity (Fig. 6) and more latent heat over the tropical Indian Ocean (Figs. 2a–e).

4. Relative contributions of dynamic and thermodynamic components to SASM precipitation changes

A column-integrated moisture budget method is used to understand the physical processes related to the increase in the SASM precipitation. Figure 7 shows the model-simulated precipitation (black bars), the sum of precipitation (light blue bars) calculated based on the moisture budget Eq. (5) and its different contributors. With the warming, the enhanced precipitation is mainly due to the increase in moisture convergence (MC). The MC increases from 0.19, 0.30, 0.49, 0.71, and 0.98 mm day^{-1} when the warming from 1.5° to 5°C, which well corresponds to the precipitation changes. The spatial pattern of changes in MC is also similar to the precipitation change (not shown), which supports the estimate from the budget method that MC plays a dominant role in the changes in SASM precipitation. The contribution of horizontal advection (AD) is positive but much smaller than that of the MC. Evaporation makes a slight positive contribution to the increased SASM precipitation, which is different from the previous conclusion about the significant positive contribution of evaporation to global monsoon precipitation increase (Hsu et al. 2012, 2013). This may reflect a unique regional feature in the SASM region; the latest works by Chen et al. (2020) and Jin et al. (2020) also found this phenomenon based on CMIP6 models. The precipitation changes based on the moisture budget method are quite consistent with the model-simulated changes of SASM precipitation under global warming, although there is a small difference between them. The difference may be due to a not real equilibrium state when the warming is small since the budget equation is assumed to apply in the equilibrium state. The mass discontinuity at the top of the troposphere may also contribute to the residual.

Investigating the role of the dynamic (DY) and thermodynamic (TH) component in the changes of MC is crucial to

TABLE 1. Percentage changes for per degree warming (% °C^{-1}) in the SASMI, the SASM area-averaged (0°–20°N, 60°–100°E) precipitation (SASM-Pr), precipitable water (SASM-Prw), static stability (potential temperature $\theta_{400\text{–}300\,\text{hPa}} - \theta_{1000\text{–}850\,\text{hPa}}$; SASM-Stability), and globally averaged precipitation (Global-Pr), precipitable water (Global-Prw), and static stability (Global-Stability) in JJA when global warming is at 2°, 3°, 4°, and 5°C above the preindustrial level, respectively; $\Delta_{2°C}$, $\Delta_{3°C}$, $\Delta_{4°C}$, and $\Delta_{5°C}$ denote 2°C minus current climate, 3°C minus 2°C, 4°C minus 3°C, and 5°C minus 4°C, respectively.

	$\Delta_{2°C}$	$\Delta_{3°C}$	$\Delta_{4°C}$	$\Delta_{5°C}$
SASMI	−2.7	−3.2	−3.6	−3.3
SASM-Pr	3.5	4.2	3.6	3.4
SASM-Prw	7.1	7.2	6.9	6.1
SASM-Stability	14.0	9.8	5.9	3.2
Global-Pr	1.6	1.3	1.1	1.1
Global-Prw	7.1	7.2	7.1	6.8
Global-Stability	2.3	2.2	2.1	1.9

understand the physical mechanisms of the precipitation changes. Figure 8 shows their separate contributions under different warming levels. The TH due to the increased atmospheric water vapor plays a dominant role in enhancing the MC, while the DY basically (except 1.5°C) makes a negative contribution to the increase of MC, with weaker strength than the TH. The DY will quasi-linearly decrease by 0.22, 0.38, 0.31, and 0.42 mm day^{-1} from 1° to 2°C, from 2° to 3°C, from 3° to 4°C, and from 4° to 5°C, respectively. The weakened SASM circulation favors an anomalous weakened convergence in the SASM region, which leads to the negative contribution of the DY. The TH will quasi-linearly increase by 0.55, 0.58, 0.63, and 0.59 mm day^{-1} from 1° to 2°C, from 2° to 3°C, from 3° to 4°C, and from 4° to 5°C, respectively. The strength of the TH is about twice that of the DY, which shows the dominant positive effect of the TH on the enhanced precipitation. Besides, the changes in the nonlinear term (NL) are small and negligible.

Since the column-integrated budget could not completely separate the contribution from the thermodynamic and dynamic component to the precipitation changes, we also use a simplified moisture budget (Fig. 9) method proposed by Huang et al. (2013) to estimate the contribution from different components. The simplified method can directly manifest the DY and TH contributions to precipitation changes over tropical regions. Based on Fig. 9, the thermodynamic component $\{-[1/(\rho g)](\Delta q_s \overline{\omega})\}$ will quasi-linearly increase by 0.35, 0.35, 0.40, and 0.37 mm day^{-1} from 1° to 2°C, from 2° to 3°C, from 3° to 4°C, and from 4° to 5°C, respectively. And the thermodynamic component plays a dominant role in the SASM precipitation increases. The dynamic component $\{-[1/(\rho g)](\overline{q}_s \Delta\omega)\}$ related to the weakening of the 500-hPa vertical velocity makes a negative contribution to the precipitation increase, with a quasi-linearly decreasing rate by 0.10, 0.08, 0.08, and 0.09 mm day^{-1} from 1° to 2°C, from 2° to 3°C, from 3° to 4°C, and from 4° to 5°C, respectively. The residual of the budget shows a little increase with warming, which may be due to the not real equilibrium state. Besides, the 500-hPa vertical velocity may not perfectly reflect the convergence, which also partly contributes to the residual. The main conclusions from this simplified method support the results from the column-integrated method. Both moisture budgets highlight the essential effect of the quasi-linearly increased water vapor (thermodynamic) related to global warming on the SASM precipitation increase, while the weakened SASM circulation makes a negative effect.

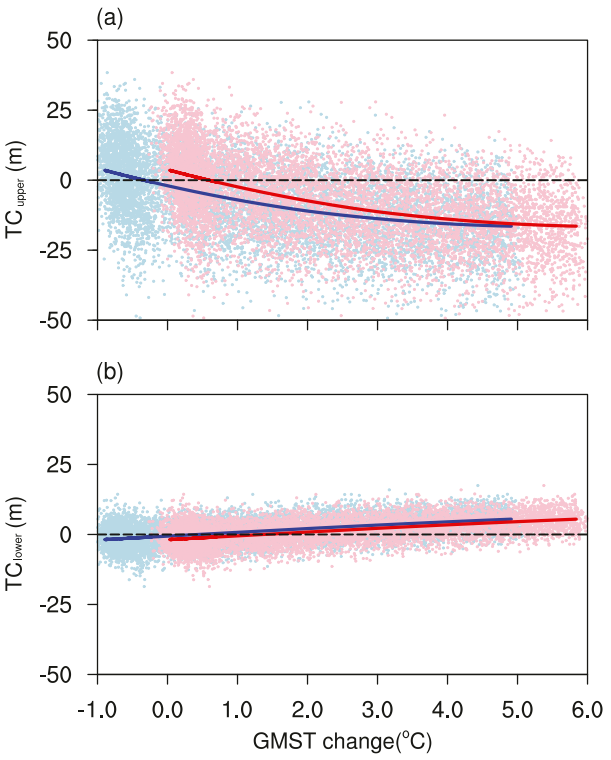

FIG. 5. As in Fig. 4, but for north–south land–sea thermal contrast (m) in the (a) upper (TC_{upper}) and (b) lower (TC_{lower}) troposphere and GMST (°C).

5. Conclusions

The large-ensemble runs of CanESM2 are used to investigate the link between the SASM changes and different global warming levels. With the warming, the large-ensemble mean SASM precipitation is projected to increase quasi-linearly at a rate of ~4% K^{-1}, which is much larger than the global mean precipitation increases. The increase of precipitation is mainly seen over the ocean but not over land in the SASM region. The SASM precipitable water will increase quasi-linearly at a rate of ~7% K^{-1} that is similar to the global mean, which is conducive to precipitation quasi-linearly increase. The static stability will increase at a larger rate of 3%–14% K^{-1} than the global mean, which is mainly due to the faster warming in the upper-level troposphere than that at the lower level. On the other hand, the SASM circulation is projected to weaken quasi-linearly with global warming, with the decrease of both lower- and upper-level winds. The anomalous double low-level anticyclones alongside the equatorial Indian Ocean contribute

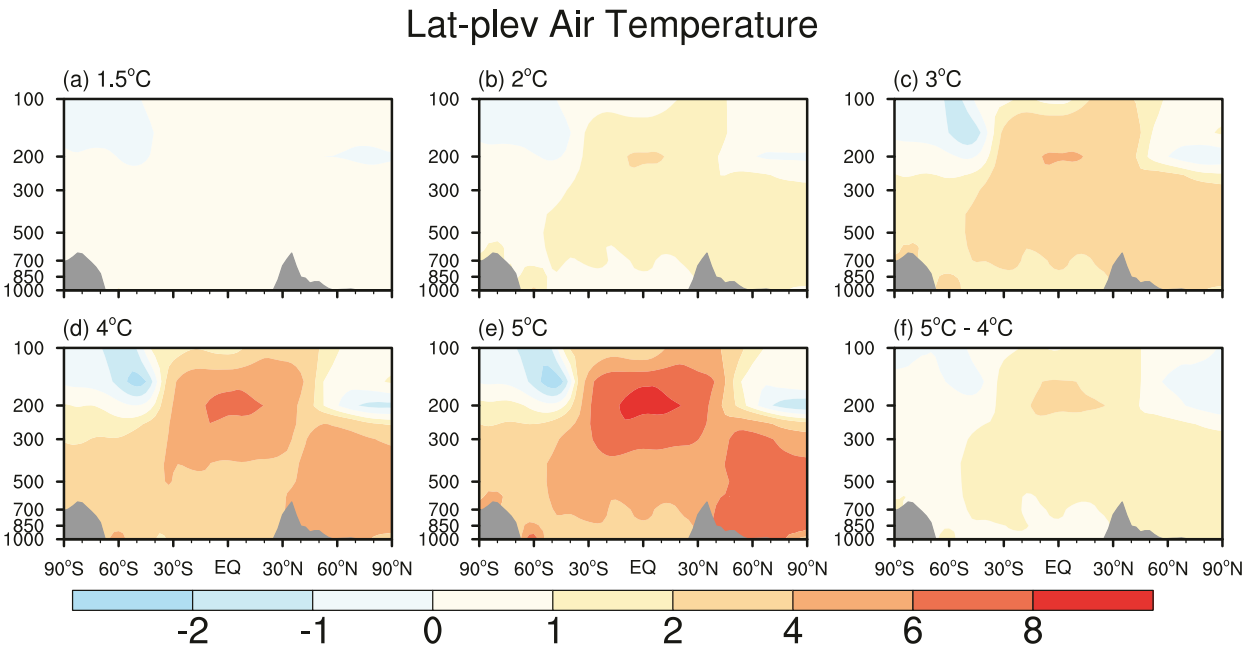

FIG. 6. As in Figs. 2a–f, but for zonally averaged (60°–100°E) air temperature (°C). The changes in air temperature are significant nearly at each grid point. Dark gray shadings denote the orography.

to the changes in lower-level circulation. The anomalous water vapor transport belt over northern India passing through the Somali jet is conducive to the local precipitation increase. Both global warming induced upper-level warming and convection induced latent heat release contribute to the fast increase of temperature in the upper-level troposphere over the tropical Indian Ocean, thus leading to the decrease of tropical easterly jet and large-scale upper-level land–sea thermal contrast (TC_{upper}) between the Asian continent and the tropical Indian Ocean. Lower-level land–sea thermal contrast (TC_{lower}) slightly increases with global warming, which is related to faster near-surface air warming over land than the sea according to the difference in heat capacity.

A column-integrated moisture budget method was used to estimate the relative contributions of dynamic and thermodynamic components to future SASM precipitation changes. Both horizontal advection (AD) and moisture convergence (MC) show positive contributions to the SASM precipitation increase, and the effect of the MC plays a dominant role. The contribution of evaporation is small over the SASM region all the time, which is consistent with Jin et al. (2020). The decomposition of the MC shows that the thermodynamic component (atmospheric water vapor) has a positive contribution to the SASM precipitation increase, which is consistent with previous works (e.g., Endo and Kitoh 2014; Li et al. 2015).

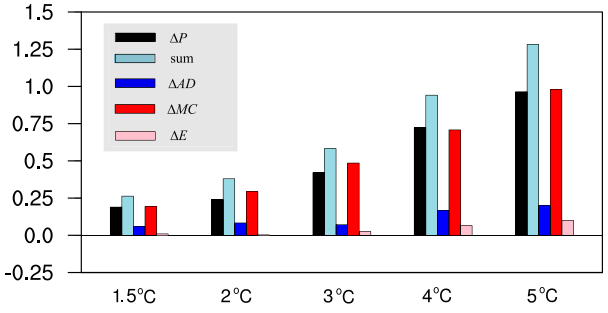

FIG. 7. Column-integrated moisture budget diagnosis of the SASM precipitation (0°–20°N, 60°–100°E) change under different global warming levels based on the 50-run ensemble mean of CanESM2. Black, light blue, blue, red, and pink bars denote the model-simulated precipitation changes (ΔP; m day^{-1}), diagnostic precipitation changes [sum; mm day^{-1}; the sum of the right-hand side of Eq. (4)], horizontal advection changes (ΔAD; mm day^{-1}), moisture convergence changes (ΔMC; mm day^{-1}), and evaporation changes (ΔE; mm day^{-1}), respectively.

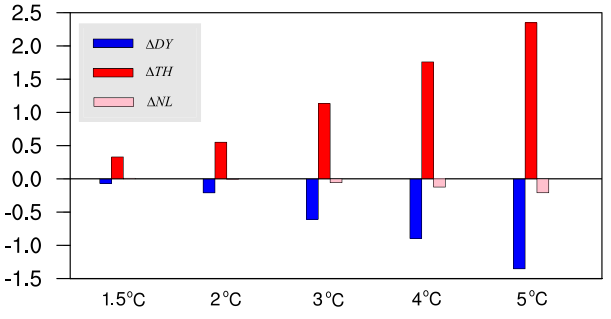

FIG. 8. As in Fig. 7, but for the decomposition results of moisture convergence (ΔMC). Blue, red, and pink bars denote the dynamic component changes (ΔDY; mm day^{-1}), thermodynamic component changes (ΔTH; mm day^{-1}), and nonlinear component changes (ΔNL; mm day^{-1}), respectively.

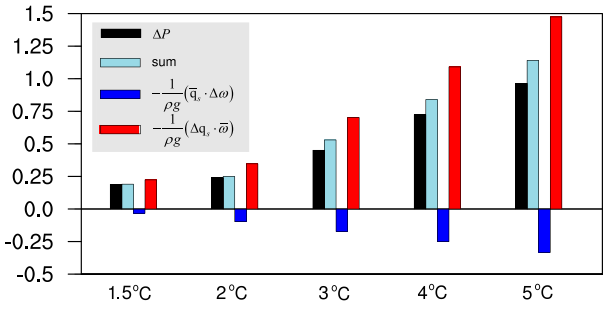

FIG. 9. Simplified moisture budget diagnosis of the SASM precipitation (0°–20°N, 60°–100°E) change under different global warming levels based on the 50-run ensemble mean of CanESM2. Black, light blue, blue, and red bars denote the model-simulated precipitation changes (ΔP; mm day^{-1}), diagnostic precipitation changes [sum; mm day^{-1}; the sum of the right-hand side of Eq. (11)], dynamic component changes $\{-[1/(\rho g)](\overline{q}_s\Delta\omega)$; mm day$^{-1}\}$, and thermodynamic component changes $\{-[1/(\rho g)](\Delta q_s\overline{\omega})$; mm day$^{-1}\}$, respectively.

In contrast, the dynamic component (circulation) has a negative contribution to the SASM precipitation increase. A simplified water vapor budget further supports these conclusions. Interestingly, both methods show that the thermodynamic (dynamic) component will quasi-linearly increase (decrease) under global warming, which well corresponds to the quasi-linearly enhanced (weakened) SASM precipitation (circulation).

Our work shows that the SASM changes at different warming levels may roughly linearly scale with the GMST increases, providing a new insight about the relation between the SASM changes and global warming. What we need to note is that these results are obtained based on only one large-ensemble model CanESM2. The model results show slight differences with some previous studies based on CMIP5 (e.g., Turner and Annamalai 2012; IPCC 2013) and CMIP6 (Wang et al. 2020a,b), including the distribution of anomalous precipitation center and the changes in the circulation intensity. Zhang and Zhou (2021) compared simulations using different modeling strategies at low warming levels and highlighted the methodological uncertainties in the projection. Hence, the quantified link between the SASM changes and the GMST increase needs to be further investigated with more climate models.

Acknowledgments. We thank the two anonymous reviewers for their valuable comments and suggestions, which helped to improve the manuscript. We also thank Prof. P.-C. Hsu and Y. H. Wang for the helpful discussion. This study was supported by the National Science Foundation of China (42025503) and the National Key R&D Program of China (2018YFA0605604). TL was supported by NSF AGS-2006553 and NOAA NA18OAR4310298. The observation datasets are available from https://psl.noaa.gov/data/gridded/index.html and https://www.ecmwf.int/en/forecasts/datasets/reanalysis-datasets/era-interim. The CanESM2 data are available from the government of Canada's open data portal http://open.canada.ca/data/en/dataset/aa7b6823-fd1e-49ff-a6fb-68076a4a477c.

REFERENCES

Adler, R. F., and Coauthors, 2003: The version 2 Global Precipitation Climatology Project (GPCP) monthly precipitation analysis (1979–present). *J. Hydrometeor.*, **4**, 1147–1167, https://doi.org/10.1175/1525-7541(2003)004<1147:TVGPCP>2.0.CO;2.

Allen, M. R., and W. J. Ingram, 2002: Constraints on future changes in climate and the hydrologic cycle. *Nature*, **419**, 228–232, https://doi.org/10.1038/nature01092.

Annamalai, H., J. Hafner, K. P. Sooraj, and P. Pillai, 2013: Global warming shifts monsoon circulation, drying South Asia. *J. Climate*, **26**, 2701–2718, https://doi.org/10.1175/JCLI-D-12-00208.1.

Arora, V. K., and G. J. Boer, 2010: Uncertainties in the 20th century carbon budget associated with land use change. *Global Change Biol.*, **16**, 3327–3348, https://doi.org/10.1111/j.1365-2486.2010.02202.x.

——, and Coauthors, 2009: The effect of terrestrial photosynthesis down-regulation on the 20th century carbon budget simulated with the CCCma Earth System Model. *J. Climate*, **22**, 6066–6088, https://doi.org/10.1175/2009JCLI3037.1.

——, and Coauthors, 2011: Carbon emission limits required to satisfy future representative concentration pathways of greenhouse gases. *Geophys. Res. Lett.*, **38**, L05805, https://doi.org/10.1029/2010GL046270.

Bhowmick, M., S. Sahany, and S. K. Mishra, 2019: Projected precipitation changes over the South Asian region for every 0.5°C increase in global warming. *Environ. Res. Lett.*, **14**, 054005, https://doi.org/10.1088/1748-9326/ab1271.

Bollasina, M. A., Y. Ming, and V. Ramaswamy, 2011: Anthropogenic aerosols and the weakening of the South Asian summer monsoon. *Science*, **334**, 502–505, https://doi.org/10.1126/science.1204994.

Chen, X., and T. Zhou, 2015: Distinct effects of global mean warming and regional sea surface warming pattern on projected uncertainty in the South Asian summer monsoon. *Geophys. Res. Lett.*, **42**, 9433–9439, https://doi.org/10.1002/2015GL066384.

Chen, Z., T. Zhou, L. Zhang, X. Chen, W. Zhang, and J. Jiang, 2020: Global land monsoon precipitation changes in CMIP6 projections. *Geophys. Res. Lett.*, **47**, e2019GL086902, https://doi.org/10.1029/2019GL086902.

Cherchi, A., A. Alessandri, S. Masina, and A. Navarra, 2011: Effects of increased CO_2 levels on monsoons. *Climate Dyn.*, **37**, 83–101, https://doi.org/10.1007/s00382-010-0801-7.

Chevuturi, A., N. P. Klingaman, A. G. Turner, and S. Hannah, 2018: Projected changes in the Asian-Australian monsoon region in 1.5°C and 2.0°C global-warming scenarios. *Earth's Future*, **6**, 339–358, https://doi.org/10.1002/2017EF000734.

Chou, C., J. D. Neelin, C. A. Chen, and J. Y. Tu, 2009: Evaluating the "rich-get-richer" mechanism in tropical precipitation change under global warming. *J. Climate*, **22**, 1982–2005, https://doi.org/10.1175/2008JCLI2471.1.

Christensen, J. H., and Coauthors, 2013: Climate phenomena and their relevance for future regional climate change. *Climate Change 2013: The Physical Science Basis*, T. F. Stocker et al., Eds., Cambridge University Press, 1217–1308.

Chung, C. E., and V. Ramanathan, 2007: Relationship between trends in land precipitation and tropical SST gradient. *Geophys. Res. Lett.*, **34**, L16809, https://doi.org/10.1029/2007GL030491.

Cleveland, W. S., 1979: Robust locally weighted regression and smoothing scatterplots. *J. Amer. Stat. Assoc.*, **74**, 829–836, https://doi.org/10.1080/01621459.1979.10481038.

Dai, A., H. Li, Y. Sun, L. C. Hong, C. Chou, and T. Zhou, 2013: The relative roles of upper and lower tropospheric thermal contrasts and tropical influences in driving Asian summer monsoons.

J. Geophys. Res., **118**, 7024–7045, https://doi.org/10.1002/jgrd.50565.

Dee, D. P., and Coauthors, 2011: The ERA-Interim reanalysis: Configuration and performance of the data assimilation system. *Quart. J. Roy. Meteor. Soc.*, **137**, 553–597, https://doi.org/10.1002/qj.828.

Deser, C., and Coauthors, 2020: Insights from Earth system model initial-condition large ensembles and future prospects. *Nat. Climate Change*, **10**, 277–286, https://doi.org/10.1038/s41558-020-0731-2.

Douville, H., J.-F. Royer, J. Polcher, P. Cox, N. Gedney, D. B. Stephenson, and P. J. Valdes, 2000: Impact of CO_2 doubling on the Asian summer monsoon: Robust versus model-dependent responses. *J. Meteor. Soc. Japan*, **78**, 421–439, https://doi.org/10.2151/jmsj1965.78.4_421.

Endo, H., and A. Kitoh, 2014: Thermodynamic and dynamic effects on regional monsoon rainfall changes in a warmer climate. *Geophys. Res. Lett.*, **41**, 1704–1711, https://doi.org/10.1002/2013GL059158.

Fyfe, J. C., and Coauthors, 2017: Large near-term projected snowpack loss over the western United States. *Nat. Commun.*, **8**, 14 996, https://doi.org/10.1038/ncomms14996.

Gautam, R., N. C. Hsu, K. M. Lau, and M. Kafatos, 2009: Aerosol and rainfall variability over the Indian monsoon region: Distributions, trends and coupling. *Ann. Geophys.*, **27**, 3691–3703, https://doi.org/10.5194/angeo-27-3691-2009.

Goswami, B. N., and P. K. Xavier, 2005: ENSO control on the South Asian monsoon through the length of the rainy season. *Geophys. Res. Lett.*, **32**, L18717, https://doi.org/10.1029/2005GL023216.

——, V. Krishnamurthy, and H. Annmalai, 1999: A broad-scale circulation index for the interannual variability of the Indian summer monsoon. *Quart. J. Roy. Meteor. Soc.*, **125**, 611–633, https://doi.org/10.1002/qj.49712555412.

Held, I. M., and B. J. Soden, 2006: Robust responses of the hydrological cycle to global warming. *J. Climate*, **19**, 5686–5699, https://doi.org/10.1175/JCLI3990.1.

Hsu, P.-C., T. Li, J. J. Luo, H. Murakami, A. Kitoh, and M. Zhao, 2012: Increase of global monsoon area and precipitation under global warming: A robust signal? *Geophys. Res. Lett.*, **39**, L6701, https://doi.org/10.1029/2012GL051037.

——, ——, H. Murakami, and A. Kitoh, 2013: Future change of the global monsoon revealed from 19 CMIP5 models. *J. Geophys. Res.*, **118**, 1247–1260, https://doi.org/10.1002/jgrd.50145.

Huang, P., and S. P. Xie, 2015: Mechanisms of change in ENSO-induced tropical Pacific rainfall variability in a warming climate. *Nat. Geosci.*, **8**, 922–926, https://doi.org/10.1038/ngeo2571.

——, ——, K. Hu, G. Huang, and R. Huang, 2013: Patterns of the seasonal response of tropical rainfall to global warming. *Nat. Geosci.*, **6**, 357–361, https://doi.org/10.1038/ngeo1792.

Huang, X., and Coauthors, 2020a: The recent decline and recovery of Indian summer monsoon rainfall: Relative roles of external forcing and internal variability. *J. Climate*, **33**, 5035–5060, https://doi.org/10.1175/JCLI-D-19-0833.1.

——, and Coauthors, 2020b: South Asian summer monsoon projections constrained by the interdecadal Pacific oscillation. *Sci. Adv.*, **6**, eaay6546, https://doi.org/10.1126/sciadv.aay6546.

IPCC, 2013: *Climate Change 2013: The Physical Science Basis*. Cambridge University Press, 1535 pp., https://doi.org/10.1017/CBO9781107415324.

Jin, C., B. Wang, and J. Liu, 2020: Future changes and controlling factors of the eight regional monsoons projected by CMIP6 models. *J. Climate*, **33**, 9307–9326, https://doi.org/10.1175/JCLI-D-20-0236.1.

Jin, Q., and C. Wang, 2017: A revival of Indian summer monsoon rainfall since 2002. *Nat. Climate Change*, **7**, 587–594, https://doi.org/10.1038/nclimate3348.

Kalnay, E., and Coauthors, 1996: The NCEP/NCAR 40-Year Reanalysis Project. *Bull. Amer. Meteor. Soc.*, **77**, 437–471, https://doi.org/10.1175/1520-0477(1996)077<0437:TNYRP>2.0.CO;2.

Lau, K., and Coauthors, 2008: The Joint Aerosol–Monsoon Experiment: A new challenge for monsoon climate research. *Bull. Amer. Meteor. Soc.*, **89**, 369–384, https://doi.org/10.1175/BAMS-89-3-369.

Lee, D., S.-K. Min, E. Fischer, H. Shiogama, I. Bethke, L. Lierhammer, and J. F. Scinocca, 2018: Impacts of half a degree additional warming on the Asian summer monsoon rainfall characteristics. *Environ. Res. Lett.*, **13**, 044033, https://doi.org/10.1088/1748-9326/aab55d.

Lehner, F., C. Deser, N. Maher, J. Marotzke, E. M. Fischer, L. Brunner, R. Knutti, and E. Hawkins, 2020: Partitioning climate projection uncertainty with multiple large ensembles and CMIP5/6. *Earth Syst. Dyn.*, **11**, 491–508, https://doi.org/10.5194/esd-11-491-2020.

Li, X., and M. Ting, 2017: Understanding the Asian summer monsoon response to greenhouse warming: The relative roles of direct radiative forcing and sea surface temperature change. *Climate Dyn.*, **49**, 2863–2880, https://doi.org/10.1007/s00382-016-3470-3.

——, ——, C. Li, and N. Henderson, 2015: Mechanisms of Asian summer monsoon changes in response to anthropogenic forcing in CMIP5 models. *J. Climate*, **28**, 4107–4125, https://doi.org/10.1175/JCLI-D-14-00559.1.

Li, Z., Y. Sun, T. Li, Y. Ding, and T. Hu, 2019: Future changes in East Asian summer monsoon circulation and precipitation under 1.5 to 5°C of warming. *Earth's Future*, **7**, 1391–1406, https://doi.org/10.1029/2019EF001276.

——, W. Chen, S. Chen, Y. Sun, and D. Qian, 2021: Uncertainty of central China summer precipitation and related natural internal variability under global warming of 1°C to 3°C. *Int. J. Climatol.*, https://doi.org/10.1002/joc.7217, in press.

May, W., 2004: Potential future changes in the Indian summer monsoon due to greenhouse warming: Analysis of mechanisms in a global time-slice experiment. *Climate Dyn.*, **22**, 389–414, https://doi.org/10.1007/s00382-003-0389-2.

——, 2011: The sensitivity of the Indian summer monsoon to a global warming of 2°C with respect to pre-industrial times. *Climate Dyn.*, **37**, 1843–1868, https://doi.org/10.1007/s00382-010-0942-8.

Mitchell, D., and Coauthors, 2017: Half a degree additional warming, prognosis and projected impacts (HAPPI): Background and experimental design. *Geosci. Model Dev.*, **10**, 571–583, https://doi.org/10.5194/gmd-10-571-2017.

Mitchell, T. D., and P. D. Jones, 2005: An improved method of constructing a database of monthly climate observations and associated high-resolution grids. *Int. J. Climatol.*, **25**, 693–712, https://doi.org/10.1002/joc.1181.

Niyogi, D., C. Kishtawal, S. Tripathi, and R. S. Govindaraju, 2010: Observational evidence that agricultural intensification and land use change may be reducing the Indian summer monsoon rainfall. *Water Resour. Res.*, **46**, W03533, https://doi.org/10.1029/2008WR007082.

Parthasarathy, B., A. A. Munot, and D. R. Kothawale, 1994: All-India monthly and seasonal rainfall series: 1871–1993. *Theor. Appl. Climatol.*, **49**, 217–224, https://doi.org/10.1007/BF00867461.

Rajeevan, M., J. J. Bhate, J. D. Kale, and B. Lal, 2006: A high resolution daily gridded rainfall data for the Indian region: Analysis of break and active monsoon spells. *Curr. Sci.*, **91**, 296–306, https://www.jstor.org/stable/24094135.

Ramanathan, V. C., and Coauthors, 2005: Atmospheric brown clouds: Impacts on South Asian climate and hydrological cycle. *Proc. Natl. Acad. Sci. USA*, **102**, 5326–5333, https://doi.org/10.1073/pnas.0500656102.

Seager, R., A. Naik, and G. A. Vecchi, 2010: Thermodynamic and dynamic mechanisms for large-scale changes in the hydrological cycle in response to global warming. *J. Climate*, **23**, 4651–4668, https://doi.org/10.1175/2010JCLI3655.1.

Seneviratne, S. I., and M. Hauser, 2020: Regional climate sensitivity of climate extremes in CMIP6 vs CMIP5 multi-model ensembles. *Earth's Future*, **8**, e2019EF001474, https://doi.org/10.1029/2019EF001474.

Sooraj, K. P., P. Terray, and M. Mujumdar, 2015: Global warming and the weakening of the Asian summer monsoon circulation: Assessments from the CMIP5 models. *Climate Dyn.*, **45**, 233–252, https://doi.org/10.1007/s00382-014-2257-7.

Sperber, K. R., and Coauthors, 2013: The Asian summer monsoon: An intercomparison of CMIP5 vs. CMIP3 simulations of the late 20th century. *Climate Dyn.*, **41**, 2711–2744, https://doi.org/10.1007/s00382-012-1607-6.

Sun, Y., Y. Ding, and A. Dai, 2010: Changing links between South Asian summer monsoon circulation and tropospheric land–sea thermal contrasts under a warming scenario. *Geophys. Res. Lett.*, **37**, L02704, https://doi.org/10.1029/2009GL041662.

——, S. Dong, X. Zhang, P. A. Stott, and T. Hu, 2018: Anthropogenic influence on the heaviest June precipitation in southeastern China since 1961 [in "Explaining Extreme Events of 2017 from a Climate Perspective"]. *Bull. Amer. Meteor. Soc.*, **99** (12), S79–S83, https://doi.org/10.1175/BAMS-D-18-0114.1.

Turner, A. G., and H. Annamalai, 2012: Climate change and the South Asian summer monsoon. *Nat. Climate Change*, **2**, 587–595, https://doi.org/10.1038/nclimate1495.

Ueda, H., A. Iwai, K. Kuwako, and M. Hori, 2006: Impact of anthropogenic forcing on the Asian summer monsoon as simulated by eight GCMs. *Geophys. Res. Lett.*, **33**, L06703, https://doi.org/10.1029/2005GL025336.

von Salzen, K., and Coauthors, 2013: The Canadian fourth generation atmospheric global climate model (CanAM4). Part I: Representation of physical processes. *Atmos.–Ocean*, **51**, 104–125, https://doi.org/10.1080/07055900.2012.755610.

Wang, B., and Z. Fan, 1999: Choice of South Asian summer monsoon indices. *Bull. Amer. Meteor. Soc.*, **80**, 629–638, https://doi.org/10.1175/1520-0477(1999)080<0629:COSASM>2.0.CO;2.

——, J. Liu, H. Kim, P. Webster, and S. Yim, 2012: Recent change of the global monsoon precipitation (1979–2008). *Climate Dyn.*, **39**, 1123–1135, https://doi.org/10.1007/s00382-011-1266-z.

——, S.-Y. Yim, J.-Y. Lee, J. Liu, and K.-J. Ha, 2013: Future change of Asian-Australian monsoon under RCP 4.5 anthropogenic warming scenario. *Climate Dyn.*, **42**, 83–100, https://doi.org/10.1007/s00382-013-1769-x.

——, C. Jin, and J. Liu, 2020a: Understanding future change of global monsoons projected by CMIP6 models. *J. Climate*, **33**, 6471–6489, https://doi.org/10.1175/JCLI-D-19-0993.1.

——, and Coauthors, 2020b: Monsoons climate change assessment. *Bull. Amer. Meteor. Soc.*, **101**, E1–E19, https://doi.org/10.1175/BAMS-D-19-0335.1.

Webster, P., and S. Yang, 1992: Monsoon and ENSO: Selectively interactive system. *Quart. J. Roy. Meteor. Soc.*, **118**, 877–926, https://doi.org/10.1002/qj.49711850705.

——, V. Magaña, T. Palmer, J. Shukla, R. Tomas, M. Yanai, and T. Yasunari, 1998: Monsoons: Processes, predictability, and the prospects for prediction. *J. Geophys. Res.*, **103**, 14 451–14 510, https://doi.org/10.1029/97JC02719.

WMO, 2020: WMO statement on the state of the global climate in 2019. WMO-1248, 39 pp., https://doi.org/10.13140/RG.2.2.13705.19046.

Xavier, P. K., C. Marzin, and B. N. Goswami, 2007: An objective definition of the Indian summer monsoon season and a new perspective on the ENSO–monsoon relationship. *Quart. J. Roy. Meteor. Soc.*, **133**, 749–764, https://doi.org/10.1002/qj.45.

Xie, P., and P. A. Arkin, 1997: Global precipitation: A 17-year monthly analysis based on gauge observations, satellite estimates and numerical model outputs. *Bull. Amer. Meteor. Soc.*, **78**, 2539–2558, https://doi.org/10.1175/1520-0477(1997)078<2539:GPAYMA>2.0.CO;2.

Yang, X., and P. Huang, 2021: Restored relationship between ENSO and Indian summer monsoon rainfall around 1999/2000. *Innovation*, **2**, 100102, https://doi.org/10.1016/j.xinn.2021.100102.

Zhang, W., and T. Zhou, 2021: The effect of modeling strategies on assessments of differential warming impacts of 0.5°C. *Earth's Future*, **9**, e2020EF001640, https://doi.org/10.1029/2020EF001640.

——, ——, L. Zou, L. Zhang, and X. Chen, 2018: Reduced exposure to extreme precipitation from 0.5°C less warming in global land monsoon regions. *Nat. Commun.*, **9**, 3153–3160, https://doi.org/10.1038/s41467-018-05633-3.

Zhou, S., G. Huang, and P. Huang, 2017: Changes in the East Asian summer monsoon rainfall under global warming: Moisture budget decompositions and sources of uncertainty. *Climate Dyn.*, **51**, 1363–1373, https://doi.org/10.1007/s00382-017-3959-4.

Zhou, T., W. Zhang, L. Zhang, X. Zhang, Y. Qian, D. Peng, S. Ma, and B. Dong, 2020: The dynamic and thermodynamic processes dominating the reduction of global land monsoon precipitation driven by anthropogenic aerosols emission. *Sci. China Earth Sci.*, **63**, 919–933, https://doi.org/10.1007/s11430-019-9613-9.